Mon. Not. R. Astron. Soc. **297,** 839–848 (1998)

Digital stacking of photographic plates with SuperCOSMOS

R. A. Knox,[1] N. C. Hambly,[2] M. R. S. Hawkins[2] and H. T. MacGillivray[2]

[1]*Institute for Astronomy, University of Edinburgh, Blackford Hill, Edinburgh EH9 3HJ*
[2]*Royal Observatory, Blackford Hill, Edinburgh EH9 3HJ*

Accepted 1998 February 12. Received 1998 February 6; in original form 1997 December 5

ABSTRACT

Photographic Schmidt plates are among the most effective tools in wide-field astronomy. One of the principal difficulties of photographic plates when compared to modern detectors is lack of image depth. We present a technique for stacking plates digitized using the SuperCOSMOS microdensitometer, aimed at maximizing the signal-to-noise ratio in faint images. The efficacy of several image combination algorithms is tested by stacking plate frames in the presence of spurious images. We find that an 'average sigma clipping' type pixel rejection in conjunction with our weighting scheme is most effective in delivering a clean, high signal-to-noise ratio stack. The gain in limiting magnitude obtained from stacking is found to be consistent with that expected: $\Delta M \sim 1.5$ for a stack of 16 good-quality plates.

Key words: instrumentation: miscellaneous – methods: data analysis – techniques: image processing.

1 INTRODUCTION

Continually improving CCD technology inevitably means that the case for using photographic Schmidt plates in survey work will become progressively less compelling with time. However, the unrivalled field of view of Schmidt telescopes coupled with the advent of high-speed scanning machines such as SuperCOSMOS (Miller et al. 1992; Hambly et al. 1998) still allow Schmidt plates to provide a wealth of information in wide fields (MacGillivray & Thomson 1992). The chief disadvantage of photography compared with modern CCD imaging is that the quantum efficiency of the photographic emulsion is typically between one and two orders of magnitude smaller than that of the CCD. In this paper we address the problem of lack of depth in photographic imaging by demonstrating a technique for stacking digitized Schmidt plates. This is not a new idea – previously, plate stacking has been done both photographically (e.g. Malin 1988, and references therein) and digitally (e.g. Hawkins 1991; Kemp & Meaburn 1993; Schwartzenberg, Phillipps & Parker 1996), generally in faint galaxy and quasar projects. There are still many fields with large numbers of plates where the stacking process will yield valuable data on all manner of faint objects. In addition, where sufficient plate material exists, stacking may be done at several epochs, yielding information on time-dependent phenomena, e.g., long-term variability and proper motions. Table 1 shows a 'top ten' of United Kingdom Schmidt Telescope (UKST) fields having sufficient suitable plates for stacking in the three photographic passbands *J*, *R* and *I*. The SuperCOSMOS machine is currently scanning all the UKST survey plates (Morgan et al. 1992) and is routinely archiving pixel data for subsequent analysis. Many private projects are also underway, scanning collections of plates in small numbers of fields.

Plate stacking has been approached in several different ways in the past. In Section 2 we describe the philosophy behind our choice of technique, and the arguments behind our weighting algorithm. Section 3 goes into some detail describing the stacking procedure. Example results are shown in Section 4, and discussed in Section 5. We present our conclusions in Section 6.

2 THEORETICAL BACKGROUND AND THE STACKING TECHNIQUE

Since astrometric and photomeric data for bright objects are readily available from scans of single plates, the primary purpose of plate stacking must be to maximize the signal-to-noise ratio of faint images. We also wish to devise a stacking scheme that accounts for the often large variations in plate quality, the sources of which are many and varied (Tritton 1983), but the effects of which may be quantified by analysis of the scanned plates' pixel data. Furthermore, it is advantageous in many circumstances to implement bad-pixel rejection algorithms to avoid spurious photographic image

Table 1. 'Top ten' UKST fields for plate stacking.

Rank	Field Centre		No. of plates available (as at 4 February 1998)		
	RA	DEC	J	R	I
1	21 28	−45 00	99	100	40
2	00 54	−73 00	29	5	59
3	05 20	−66 48	2	2	67
4	18 24	−33 58	31	30	3
5	05 30	−72 12	2	2	56
6	10 38	+00 08	12	33	13
7	05 12	−70 00	37	7	3
8	20 48	−35 00	22	19	4
9	06 04	−70 00	4	6	32
10	04 20	−70 00	5	6	29

defects (e.g., due to satellite trails or emulsion flaws) propagating through the stacking procedure (note that time-dependent information, e.g., positions of high proper motion objects, will be destroyed by such rejection).

The action of photons on the photographic emulsion is to produce dark grains (after development) as a function of exposure time. The photographic process is highly non-linear (e.g., Altman 1977) – a plot of the density of dark grains versus log(exposure) typically shows a 'toe', a linear part with gradient conventionally denoted γ, and a 'shoulder' where saturation due to the finite number of available grains in the emulsion is approached. Sky-limited astronomical photographs are usually exposed so as to yield a background density towards the lower end of the linear part of the characteristic curve, along with good contrast (i.e., high γ). Plate scanning in general produces a transmission value T for each pixel. Photographic densities D are, by definition (see, e.g., Altman 1977), the logarithm of the reciprocal transmission values, i.e. $D=\log_{10}(1/T)$. Calibration of transmission T to relative intensity I is achieved via the step-wedge region of the plate, where spots of known relative intensity are exposed for the duration of the main exposure. Valid stacking procedures could be performed in T, D or I units, provided that the noise characteristics of the data in those units are correctly quantified and taken into account. However, for simplicity we ideally want to work in units whose associated error distribution is Poissonian. Then errors propagate naturally in the stacking process when adding data values.

It can be shown that a density measurement is essentially a count of the number of dark grains (Nutting 1913). Fluctuations in measured density arise both from photon shot noise and the distributions in grain size and position. While fluctuations arising from grain properties are not Gaussian, the fluctuations in observed density do follow a normal distribution closely, as may be expected from the central limit theorem. Modelling by Selwyn (1935) also predicted Gaussian behaviour for density fluctuations, with the distribution rms (henceforth σ_D) proportional to the inverse square root of the aperture size. In the specific case of the science-grade emulsions used on Schmidt plates, Furenlid, Schoening & Carder (1977) have verified the Gaussian nature of the fluctuations in D. The non-linear relationships between T and D or D and I should then lead to skewed distributions for fluctuations in T and I. Stacking in units of T or I would therefore require cumbersome non-linear weights as a function of data value to propagate the errors correctly. We therefore choose to co-add pixel data in densities $[\log_{10}(1/T)]$ and, since the associated errors are normally distributed, we can use the following simple plate-weighting algorithm.

Consider a faint image on two plates to be co-added. Plate one has background noise σ_1 and our image has signal above background H_1, with plate two having corresponding characteristics σ_2 and H_2. We shall simply add our pixel data such that

$$(-\log_{10}T)_{\rm stack}=w_1(-\log_{10}T)_1+w_2(-\log_{10}T)_2, \quad (1)$$

and define our weights such that $w_1+w_2=1$. We make the (very good) approximation for faint images that the noise is constant across the profile of the image, and find the signal-to-noise ratio at the peak of the stacked image to be

$$s{:}n=f(w_1,\,w_2)=\frac{w_1H_1+w_2H_2}{\sqrt{w_1^2\sigma_1^2+w_2^2\sigma_2^2}}, \quad (2)$$

assuming normally distributed errors adding in quadrature. Putting $w_2=1-w_1$, we maximize the signal-to-noise ratio by setting $\partial f/\partial w_1=0$ and find

$$w_1=\frac{(\sigma_2^2/H_2)}{(\sigma_1^2/H_1)+(\sigma_2^2/H_2)}=\frac{(H_1/\sigma_1^2)}{(H_1/\sigma_1^2)+(H_2/\sigma_2^2)}. \quad (3)$$

Bland-Hawthorn & Shopbell (1993) have argued that due to the presence of threshold and saturation limits in photographic emulsions, density fluctuations obey a limited Poisson distribution which introduces skewness that must be corrected for in the weights. However, since we are only concerned with enhancing faint images lying safely in the linear region of the characteristic curve (demonstrated to be least affected by this effect), we argue that this source of error is negligible for our purposes.

The weighting scheme described here optimizes the signal-to-noise ratio by taking the mean, but takes no account of potential contamination by spurious images and bad pixels. In the presence of bad data, the median is a more robust (but less efficient) estimator of the 'true' mean, and will yield a cleaner stacked image than the weighted mean but with lower signal-to-noise ratio. Tukey and others (e.g., Hoaglin, Mostleler & Tukey 1983) have developed more elaborate techniques for stacking images which provide more of the efficiency of a mean estimator while retaining the 'pixel rejection' characteristics of a robust median estimator. A detailed discussion of the theory of image stacking and these estimators in particular may be found in Carter (1993) and Irwin (1996), and references therein. Tukey's biweight function is reported to be one of the best of these robust estimators, and we apply it to our plate data as a comparison to the conventional weighted average/pixel rejection combination algorithms.

3 THE STACKING PROCEDURE

3.1 Details of pixel weighting

A high-quality plate from our stacking sample was chosen to be used as a master or reference plate. A small section (1280×1280 10-μm pixels) of the pixel data from the centre of this plate was extracted for analysis, in which five blank

regions of sky (50×50 pixels) were identified. Values of σ_D and the background density D were calculated for each individual sky region, using iterative 3σ rejection in the log T distribution to discard non-sky pixels arising from plate defects or images. The global plate value of each parameter was taken to be the median average across the sky regions.

In order to obtain a well-defined faint-image signal value (corresponding to the H parameter discussed in Section 2), a 'mini-stack' of some 50 objects near the plate limit was used. Objects lying about 1 mag above the plate limit were identified in the small (1280×1280) section of pixel data used to determine the background parameters described above. These faint images were inspected, and spurious or extended objects were rejected; in addition, the stellar magnitude parameter was examined over the full run of plates to be stacked, and any object showing variation at a level greater than 3σ above the measured plate-to-plate differences was rejected. Pixel data of the good images were then extracted, and the plate background-subtracted. Positions for these objects accurate to ~ 1 μm, calculated using the SuperCOSMOS image analysis software (e.g. Beard, MacGillivray & Thanisch 1990), were used to co-add the objects, registering the images with one another on a 1-μm grid to create a finely sampled stacked array. Orthogonal strips were extracted from the centre of this combined image, which in general fit a Gaussian profile well (Fig. 1). The average height of these Gaussian fits was taken to be our parameter H for the master plate.

Both plate stacking and the weighting technique described here require that all slave plates be re-sampled on to the coordinate system of the master plate. Standard SuperCOSMOS software achieves this by dividing each plate pixel map into a 16 by 16 grid and using all object images within each subsection to define a geometric transformation (rotation, translation and scale) between coordinate systems. The (2-cm) grid size was chosen so that jumps in pixel position across grid boundaries were limited to a small fraction of a pixel and were thus negligible compared to other sampling errors. After coordinate transformation and bilinear interpolation to re-sample the data the above analysis was then simply repeated using the same blank sky regions and faint objects on the remaining plates. The resulting σ_D and H values for each slave plate were used to assign a weight relative to the master according to equation (3).

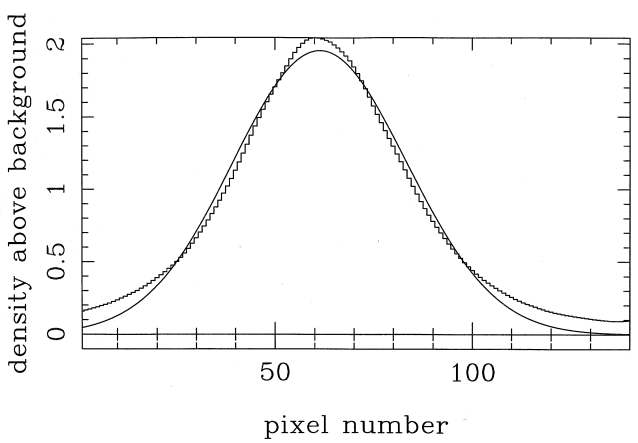

Figure 1. Histogram of a cut through a stack of faint images with a Gaussian fit overplotted.

3.2 Details of bad pixel rejection

A comprehensive set of image-combining algorithms incorporating weighting and bad pixel rejection are provided in the task 'imcombine' running under the IRAF[1] environment. In this section we present the results of using these various algorithms in conjunction with the weighting scheme described above on a set of 16 IIIaJ UKST Schmidt plates (see Table 2).

The small field used in these experiments was carefully chosen to contain plate blemishes and spurious images on one of the plates (see Fig. 2), features which would ideally be removed in any stacking process. The problem of bad pixel rejection should become progressively less serious as the number of plates to be stacked increases, and the most effective pixel-rejection algorithm may also change. The 16 plates have therefore also been analysed in substacks of four and eight plates.

The image-combination algorithms used were as follows:

(1) no rejection;
(2) median taken at each pixel;
(3) minmax rejection (one high, one low);
(4) sigma clipping (3σ rejection);
(5) average sigma clipping (3σ rejection);
(6) no weighting, no rejection;
(7) Tukey's biweight.

All except (2), (6) and (7) combined unrejected pixels by simple co-addition using weights, and any rejection was on a purely pixel-by-pixel basis, except for (5). The average sigma-clipping algorithm uses an entire strip of image data to calculate a noise model as a function of signal, which is then applied to each pixel in turn (see the online help pages for 'imcombine' for details).

Table 2. The 16 IIIaJ UK Schmidt plates used in this work.

Plate Number	Date	Exposure Time(mins)	Grade	Relative Weight
15563	24/05/93	65	bI	0.53
15795	05/10/93	60	bU	0.46
15796	06/10/93	100	bU	0.68
15801	07/10/93	90	aU	0.93
16177	06/07/94	110	a	0.84
16180	07/07/94	110	a	0.62
16183	08/07/94	110	a	0.53
16230	10/08/94	110	a	0.67
16700	29/07/95	60	aHD	0.31
16728	20/08/95	60	cXD	0.24
16731	23/08/95	60	aE	0.67
16741	25/08/95	70	aD	0.53
17117	25/05/96	90	aU	0.83
17167	07/08/96	60	aI	0.52
17173	11/08/96	60	a	1.0 (master plate)
17189	13/08/96	60	aDE	0.45

[1]IRAF is distributed by the National Optical Astronomy Observatories, which is operated by the Association of Universities for Research in Astronomy Inc., under contract with the National Science Foundation of the United States of America.

Correct application of these algorithms, of course, requires that the images have the same noise parameters. We therefore scale the data both additively and multiplicatively such that the global noise fluctuations in each plate are equal, allowing rejection of bad pixels. We note, however, that, due to sometimes large differences in seeing between plates, data in the presence of images can never be scaled to look identical. We therefore expect there to be variations in signal at the peak of faint images, inevitably resulting in a reduction of signal-to-noise ratio by the action of any pixel-rejection algorithm.

4 EXAMPLE RESULTS

The weighting algorithm was tested by stacking two plates with weights varying around those calculated using our technique. The weights we calculate were found to maximize the signal-to-noise ratio in faint images.

The relative merit of these stacking methods was assessed by considering both the signal-to-noise ratio in the resultant stack and the success of the pixel rejection in removing unwanted features. Each stack was reanalysed using the technique described in Section 3.1, and its signal-to-noise ratio was taken to be H/σ_D. The results are shown in Table 3. While the performances of the various rejection algorithms are assessed in Section 5, we answer the fundamental question of whether spurious features are likely to contaminate stacked data by simulating the action of the SuperCOSMOS image analysis software on our data. The 'pisafind' task in PISA (Draper & Eaton 1996) performs isophotal analysis on image data and is equivalent to the analogous SuperCOSMOS routine. We adopt the SuperCOSMOS norm of defining a 2.5σ detection as a signal and defining eight connected signal pixels as an object detection.

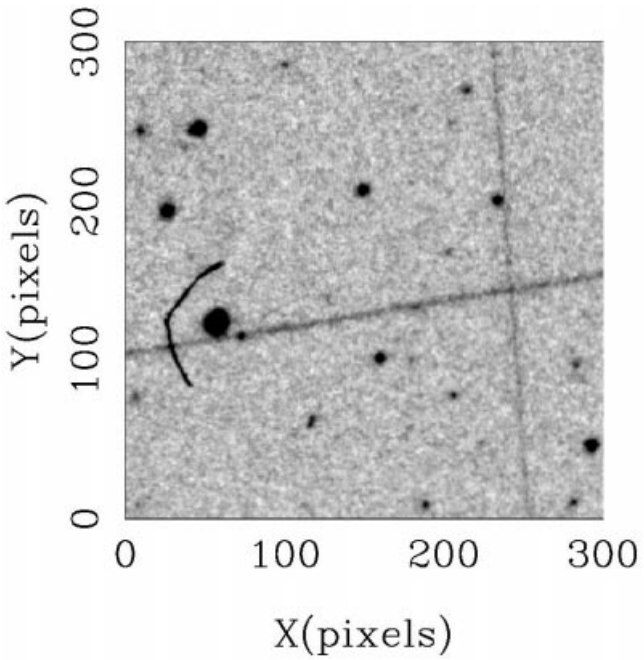

Figure 2. Pixel map of a region of plate J15796 containing two satellite trails crossing and a dust speck.

Table 3. Results of signal-to-noise ratio analysis on stacks (*note:* plate J15796 containing the image defects had a signal-to-noise ratio of 5.0 and the master plate had a signal-to-noise ratio of 8.9).

Stacking algorithm	4 plate stack s:n	8 plate stack s:n	16 plate stack s:n
(1) No rejection	12.8	18.7	23.3
(2) Median	10.3	14.9	18.1
(3) Minmax	10.3	16.6	21.4
(4) Sigma clipping	12.1	17.6	22.0
(5) Average sigma clipping	11.0	16.8	21.7
(6) No weighting, no rejection	11.1	16.8	20.9
(7) Tukey's biweight	–	–	18.8

Pixel and PISA thresholded image ellipse plots are shown for selected stacks. The results of stacking four plates are shown in Figs 3–10. The results of sigma-clipping rejection in eight-plate stacks and the full 16-plate stacks are shown in Figs 11–14. The full-stack results with no rejection are shown in Figs 15 and 16.

Certain applications of image-analysis software may require a relaxation of the criteria for object detection. Fig. 17 shows the ellipse plot for four plates stacked with no pixel rejection, with the object detection criteria relaxed to six interconnected 2σ signal detections. The result of applying the same detection criteria to a four-plate stack with average sigma-clipping rejection is shown in Fig. 18.

The weighting algorithm itself was tested by stacking the same two plates several times with various relative weightings. The signal-to-noise ratio in each resultant stack (measured as described above) is plotted against plate weight in Fig. 19, with the prediction for optimum weighting from our algorithm also plotted.

5 DISCUSSION

All rejection algorithms inevitably lead to a reduction in signal-to-noise ratios, since they can only *reduce* the signal at the peak of faint images as discussed in Section 3.2. It is clear from Table 3 that simply taking the median compromises the stack quality, while with the expected exception of minmax rejection being poor for a small number of plates the remaining rejection algorithms tend to perform equally well in terms of signal to noise.

Although Tukey's biweight is effective in removing spurious features from the stack, the stack signal-to-noise ratio is only marginally better than the median for 16 input images. The biweight technique may be improved by using a noise model to calculate sigma (as average sigma clipping does), although since the biweight always incorporates all data values into the final image (however weighted down), it cannot perform as well as an algorithm that efficiently rejects bad data outright.

Close inspection of the ellipse plots reveals that even with a four-plate stack both minmax and average sigma clipping remove both the satellite trails and the dust speck very effectively. The latter is to be preferred, however, since data are not automatically discarded, leading to increased signal-to-noise ratios in the final stack. In the case of no rejection the spurious features are propagated through the stacking procedure as expected, and are plainly visible even in the 16-plate stack in both the pixel and ellipse plots. The simple sigma-clipping algorithm is unsurprisingly very poor at rec-

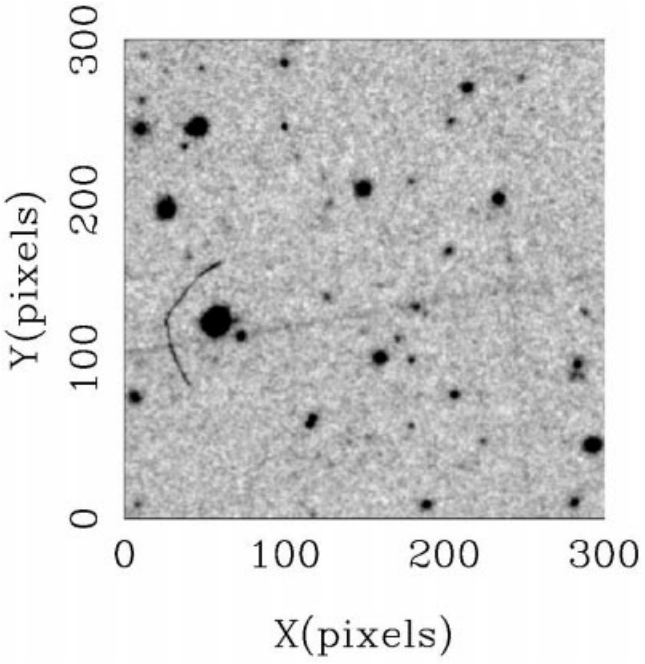

Figure 3. Four-plate-stack pixel map – no rejection used.

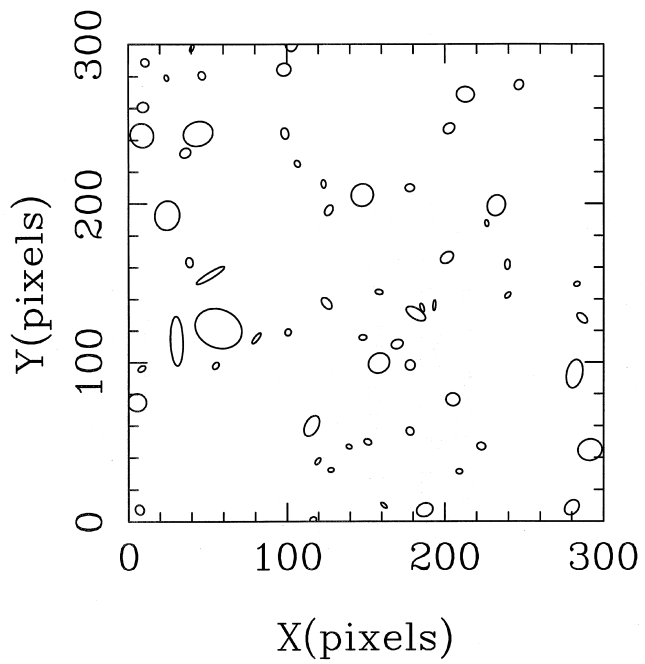

Figure 4. PISA ellipse plot of Fig. 3 pixel map – no rejection.

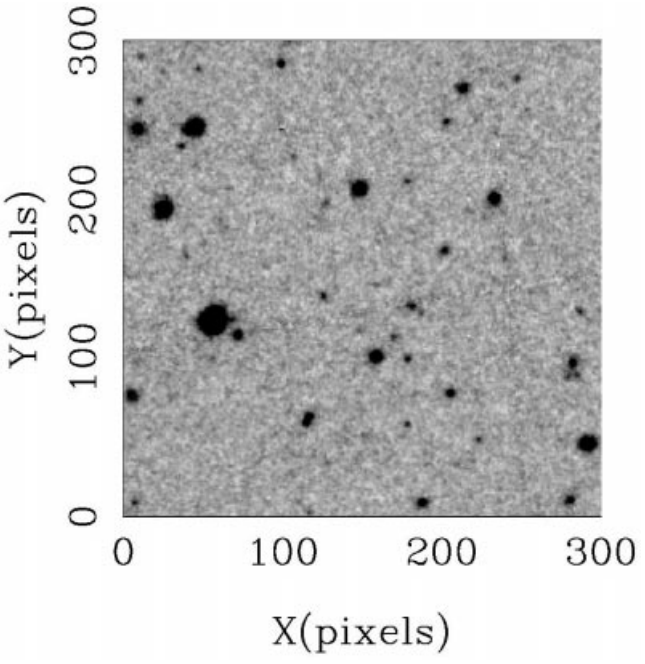

Figure 5. Four-plate-stack pixel map – average sigma-clipping rejection.

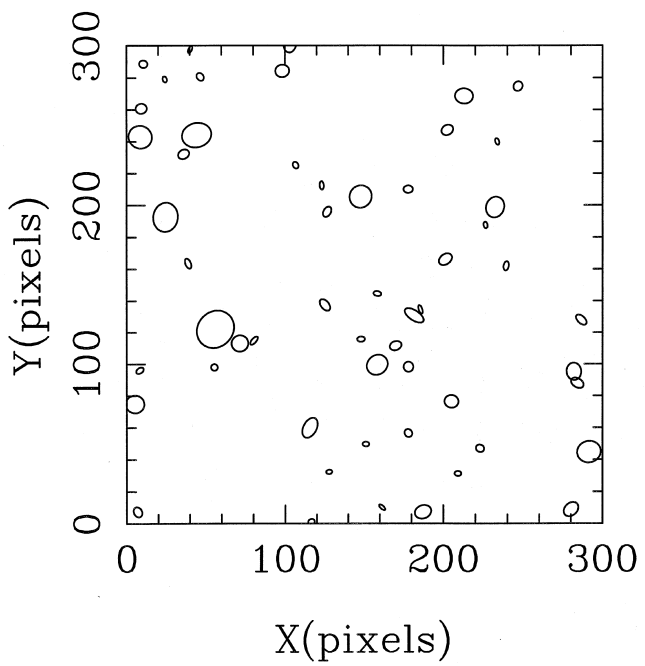

Figure 6. PISA ellipse plot of Fig. 5 pixel map – average sigma-clipping rejection.

ognizing spurious pixels in both the 4 and 8 plate stacks, although 16 plates appears to be sufficient for the 'pixel-by-pixel' technique to work adequately.

The performance of the various rejection algorithms can be assessed more quantitatively by subtracting the various stacked images from the purely weighted optimal signal-to-noise stack (number 1 in Table 3). The resulting image is zero where no pixel rejection has occurred, thus showing the regions where the rejection algorithm has been active very clearly. A 12 000-pixel area (containing no bright stars but several spurious images) has been extracted from these subtracted (16-plate) images for each rejection algorithm, plus the median and Tukey's biweight images. For a perfect algorithm, a histogram of the data values from this sub-image should have a large peak at zero, corresponding to the optimum signal-to-noise ratio where no rejection is required. There should also be a group of outlying points (generally at $\Delta D < 1$, since spurious images are more com-

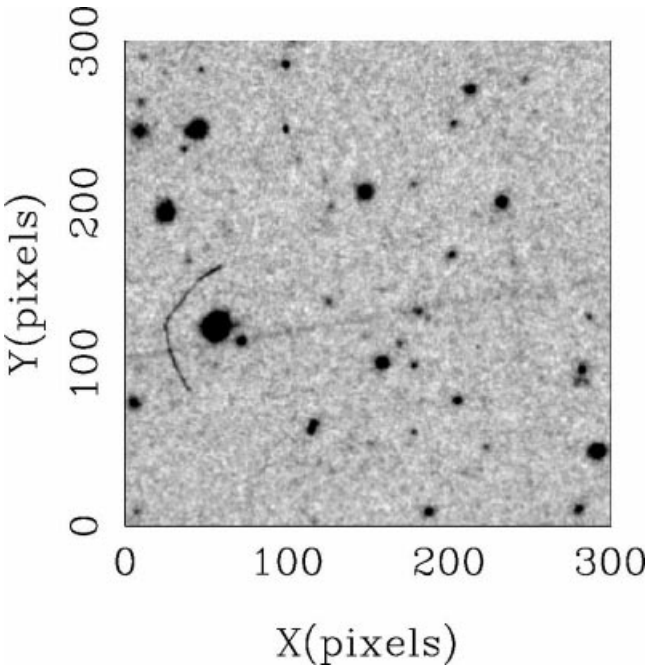

Figure 7. Four-plate-stack pixel map – sigma-clipping rejection.

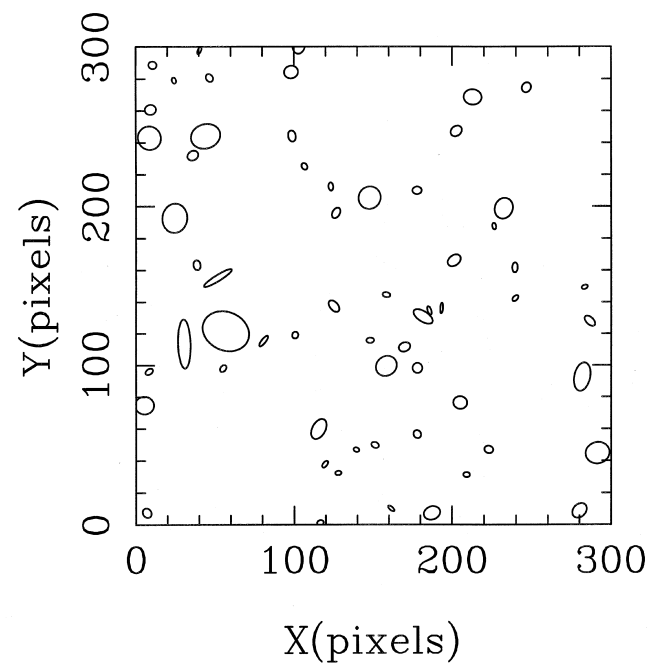

Figure 8. PISA ellipse plot of Fig. 7 pixel map – sigma-clipping rejection.

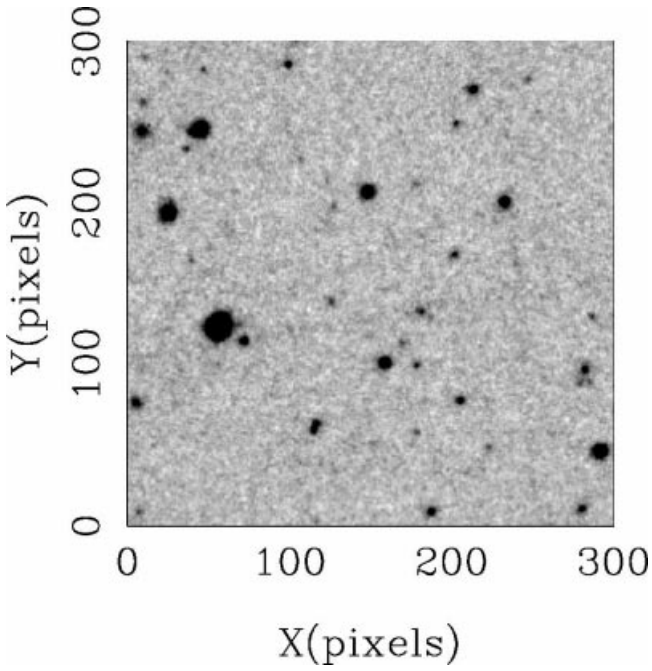

Figure 9. Four-plate-stack pixel map – minmax rejection.

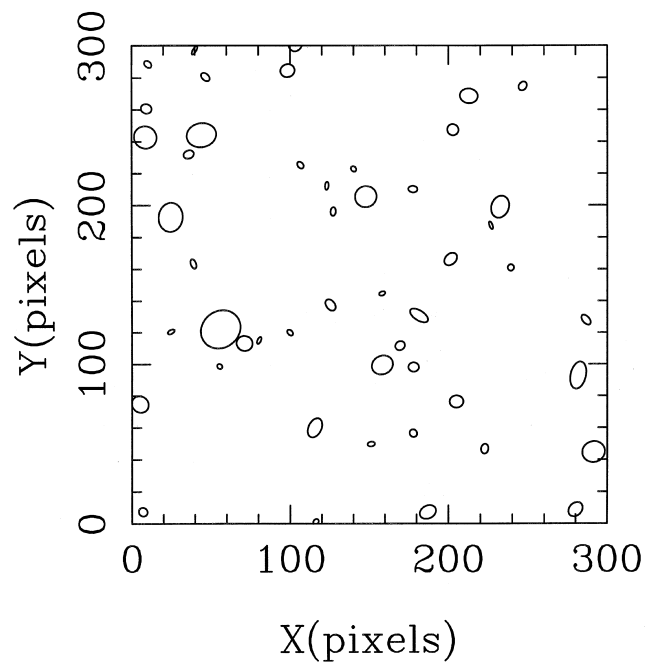

Figure 10. PISA ellipse plot of Fig. 9 pixel map – minmax rejection.

mon than emulsion scratches) where the rejection algorithm has discarded a bad data value. The 'average sigma clipping' algorithm emulates this behaviour most effectively (see Fig. 20), although the population with positive ΔD indicates that some rejection of good data is occurring (as expected for 3σ clipping). The straight sigma-clipping algorithm (Fig. 21) has been less effective in eliminating the large body of bad data at $\Delta D = -1 \times 10^{-3}$ in Fig. 20, although rejection of good data is perhaps less of a problem. The other three algorithms successfully reject deviant data (Figs 22, 23 and 24), but the plots show clearly that the stack signal-to-noise ratio has suffered as a result of the action of these algorithms, since all the good data points have been shifted to varying extents from their optimum value.

The relaxed detection criteria used in producing Fig. 17 have resulted in a clear increase in satellite trail images when compared to Fig. 4. Spurious images introduced by random sky fluctuations have also increased in number. The

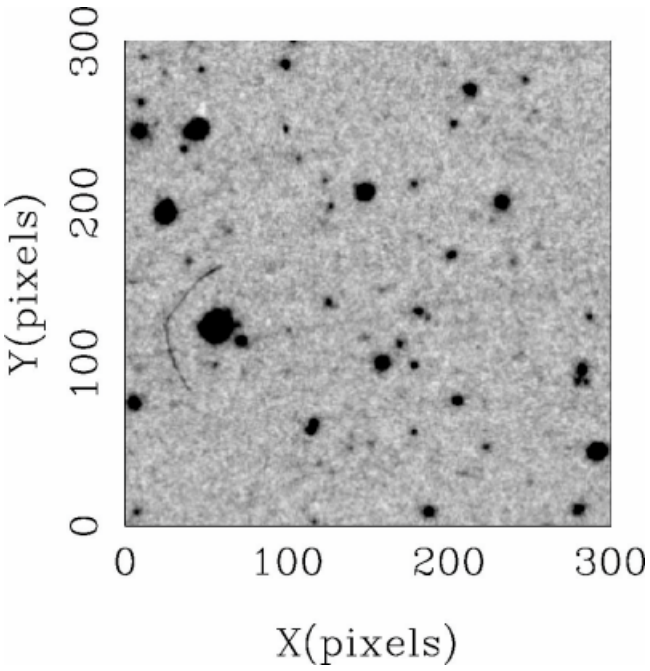

Figure 11. Eight-plate-stack pixel map – sigma clipping rejection.

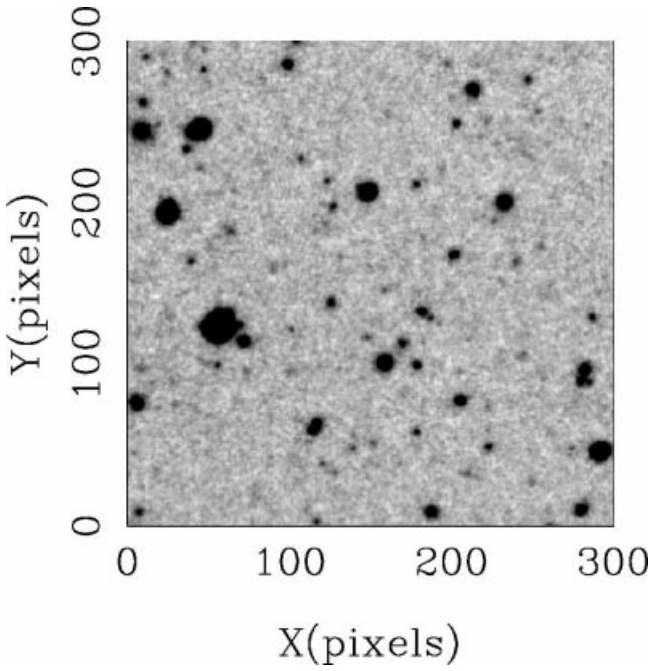

Figure 13. 16-plate-stack pixel map – sigma-clipping rejection.

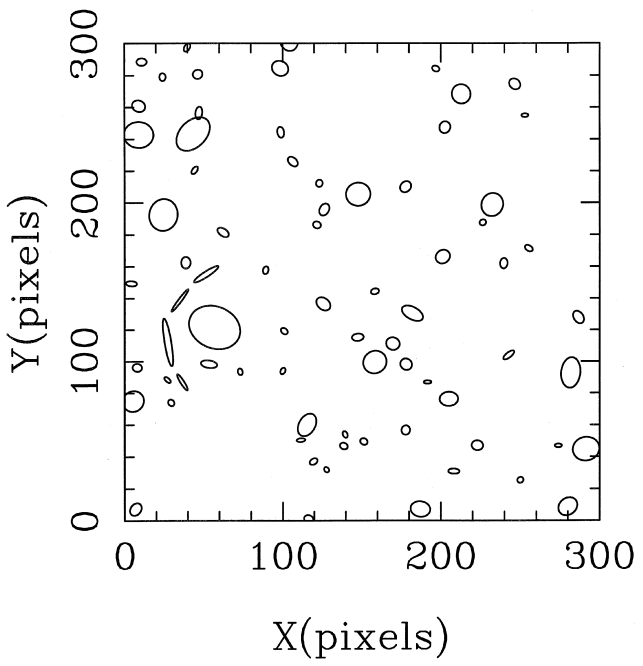

Figure 12. PISA ellipse plot of Fig. 11 pixel map – sigma-clipping rejection.

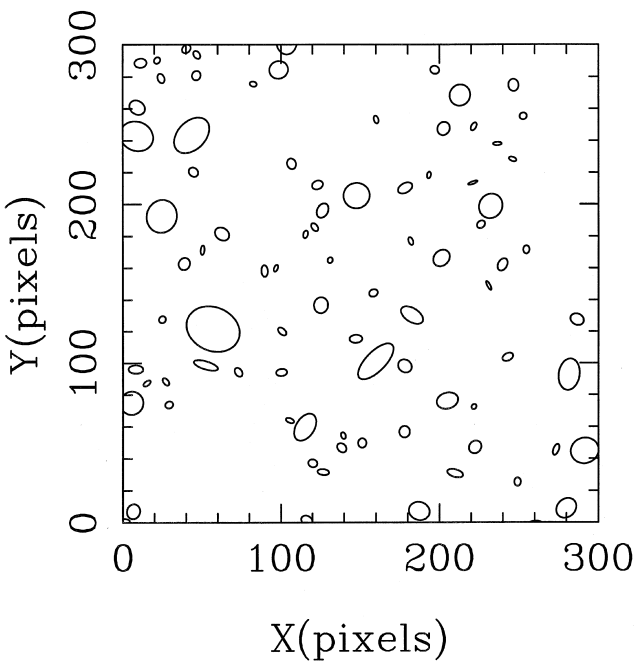

Figure 14. PISA ellipse plot of Fig. 13 pixel map – sigma-clipping rejection.

average sigma-clipping rejection performs well in eliminating bad images even in this case.

The validity of our weighting algorithm has been confirmed by our two-plate stacking experiment. Fig. 19 shows a broad maximum on the weighting axis providing optimum stack signal-to-noise ratios, which our algorithm locates successfully.

Table 3 appears to indicate that near-optimal signal-to-noise ratios are obtainable by a simple no-weighting stacking procedure. This will generally be true if, as in this paper, one is working with a universally high-quality plate collection. It should be emphasized, however, that weighting becomes increasingly important for more heterogenous plate material, where a single low-quality plate added at equal weight can seriously compromise stack quality.

Finally, we address the question of the increase in depth attainable by stacking plates. Assuming Poissonian counting errors, the signal-to-noise ratio should go as $n^{1/2}$ for identi-

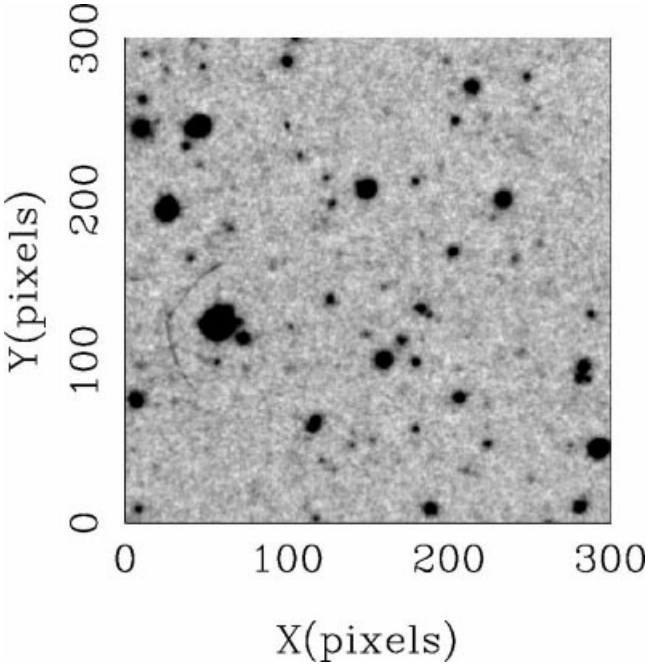

Figure 15. 16-plate-stack pixel map – no rejection.

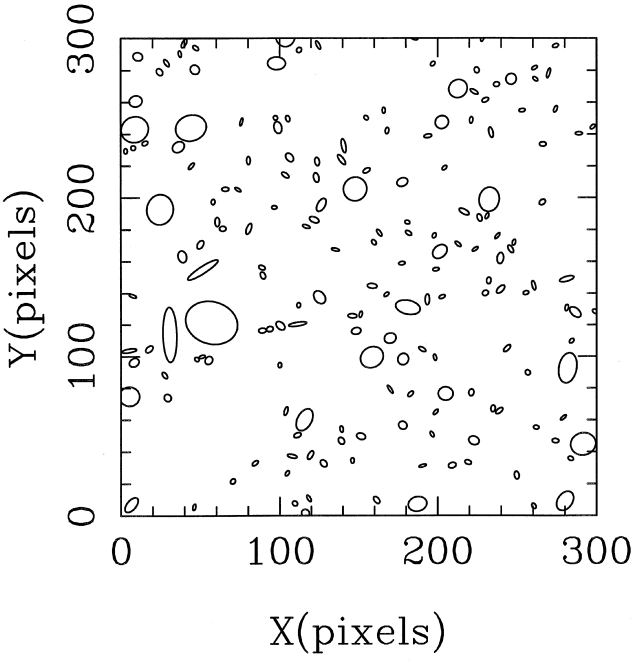

Figure 17. Four-plate-stack with no rejection PISA ellipse plot using relaxed object detection criteria.

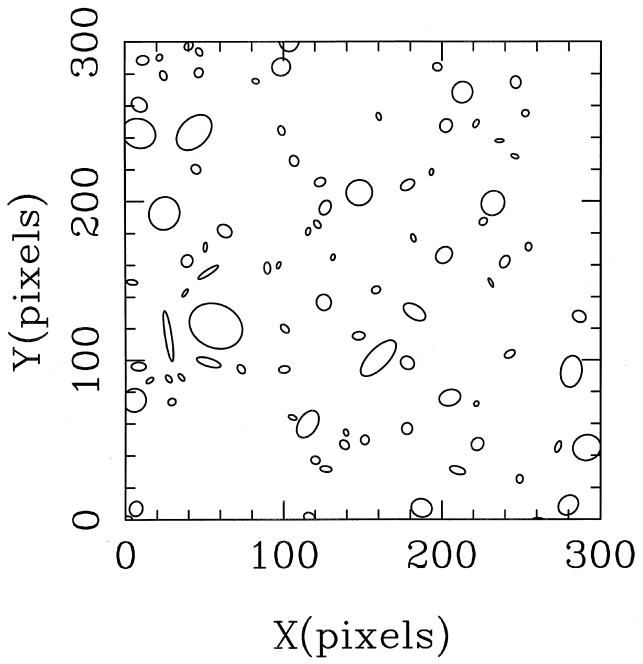

Figure 16. PISA ellipse plot of Fig. 15 pixel map – no rejection.

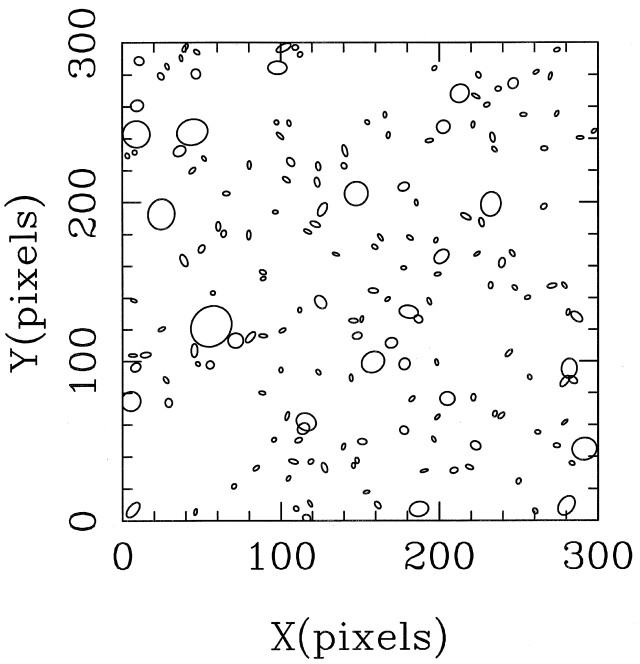

Figure 18. Four-plate-stack with average-sigma-clipping rejection PISA ellipse plot using relaxed object detection criteria.

cal plates, and therefore the increase in limiting magnitude will be $2.5 \log_{10} n^{1/2}$. In Fig. 25 we show number–magnitude counts for a single plate, and also for a four-, eight- and 16-plate stack. Taking the 100 per cent completeness limit to be the point at which a given number–magnitude count turns over, the single plate reaches $B_J \sim 22$. This is around 0.5 mag brighter than the nominal 'limiting magnitude' quoted in the UKSTU Handbook (Tritton 1983). Following an $n^{1/2}$ law, the four-, eight- and 16-plate stack limits should be $B_J^4 \sim 22.8$, $B_J^8 \sim 23.1$, $B_J^{16} \sim 23.5$ respectively. This is in good agreement with Fig. 25, given that the 16 plates in question are not identical in terms of their signal-to-noise ratios (e.g., see the relative plate weights in Table 2).

6 CONCLUSIONS

The use of any pixel-rejection algorithm leads to reduction in signal-to-noise ratio in faint images in the resultant stack;

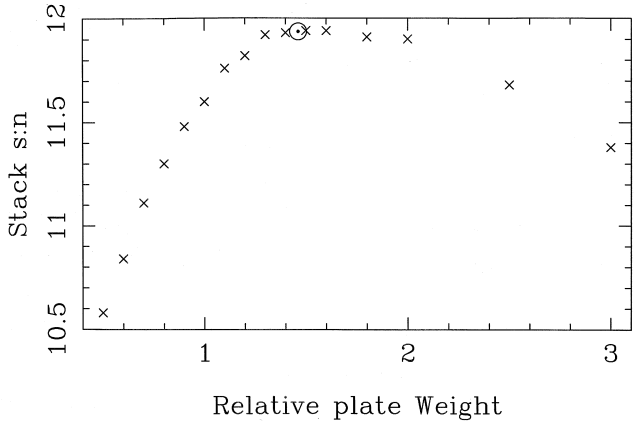

Figure 19. Resulting signal-to-noise ratio as a function of plate weighting for a stack of two test plates. Our weighting algorithm calculated an optimum relative weight shown by the dotted circle.

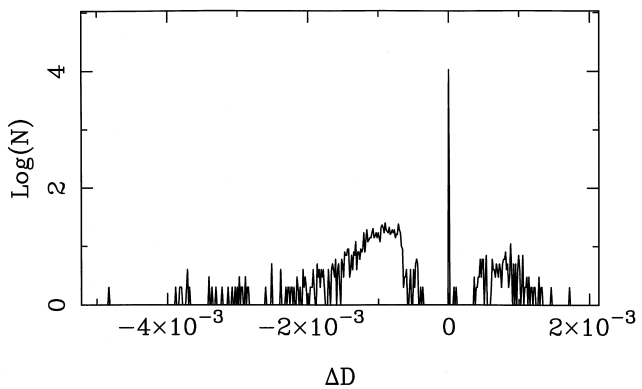

Figure 20. Rejection histogram (see text) for the 'average sigma-clipping' algorithm.

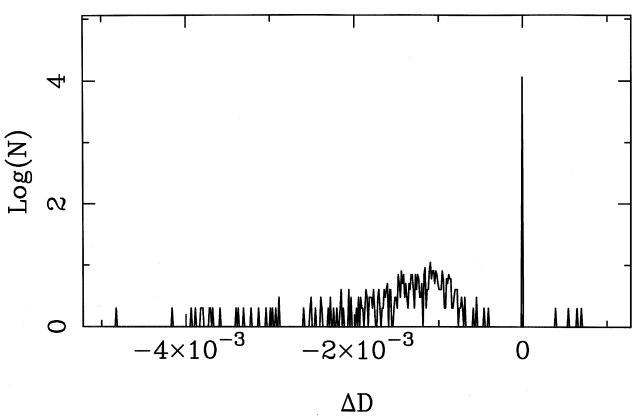

Figure 21. Sigma-clipping-rejection histogram.

thus pixel rejection should only be used in applications where spurious images are likely to pose a serious problem. In addition, while all rejection algorithms tend to work reasonably effectively for a stack of many plates, there is little need for pixel rejection in large stacks since a deviant point in one plate is unlikely to be significant when averaged into all the other plate data.

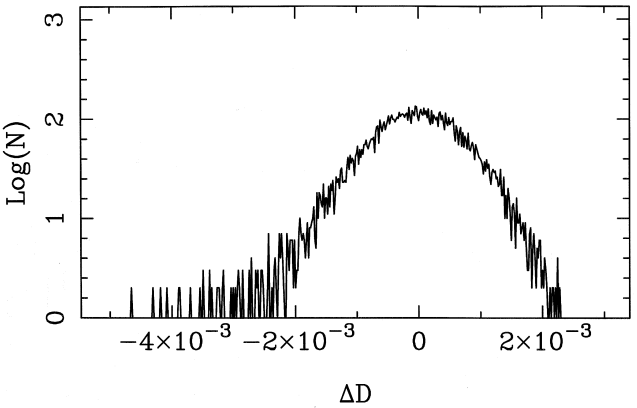

Figure 22. Median-image-rejection histogram.

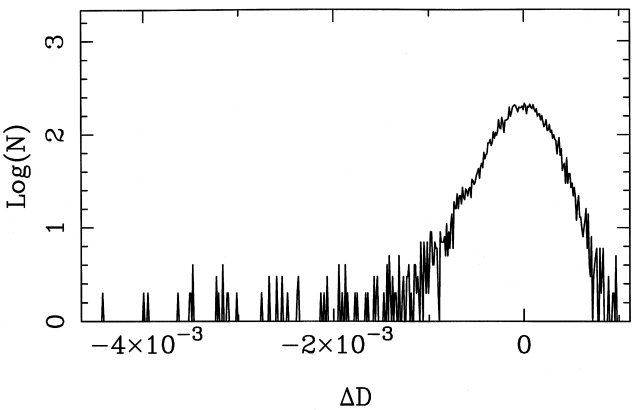

Figure 23. Minmax-rejection histogram.

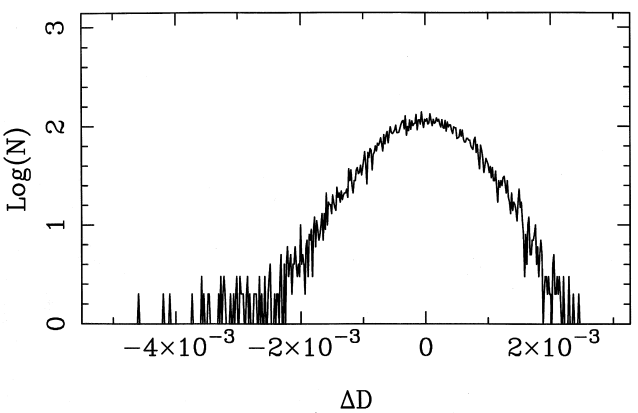

Figure 24. Tukey's biweight-rejection histogram.

The prime motivation for stacking digitized Schmidt plates is to detect faint objects over a wide field of view. The plate-stacking regime described here optimizes the signal-to-noise ratio in faint objects by analysing the noise characteristics of each plate and weighting them accordingly. We find that these weights used in conjunction with an 'average sigma clipping' bad pixel rejection algorithm yield a stacked image of near-optimal depth and free of spurious contaminant images. The gain in depth is found to be in accordance with the expected $\Delta M \sim 2.5 \log_{10} n^{1/2}$ law.

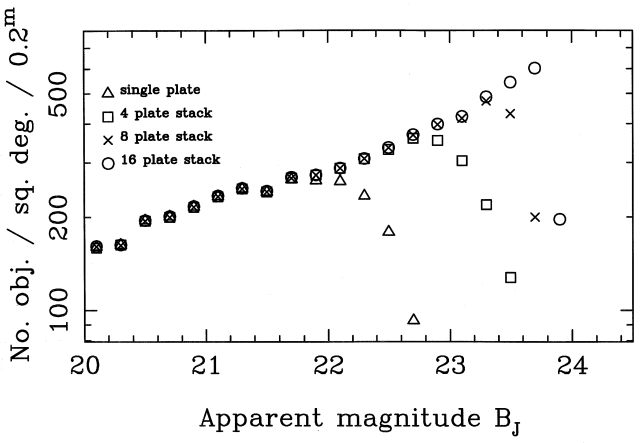

Figure 25. Number counts versus magnitude for various stacks, all with weighting but no rejection.

ACKNOWLEDGMENTS

Many people have contributed to the success of the SuperCOSMOS project. Among them are Bill Cormack, Lance Miller, Dennis Kelly, Steven Beard, Clive Davenhall, Bernard McNally, Magnus Paterson, John Cooke, Tom Paul, Joel Sylvester, Steven Stewart, Richard Bennett, John Harris and Eve Thomson. Thanks are due to David Carter for supplying the biweight code, and to Mike Irwin for helpful suggestions as a referee. We also thank the UK Schmidt Telescope Unit for obtaining and loaning the high-quality Schmidt plate material used here. Richard Knox acknowledges a PPARC post-graduate studentship.

REFERENCES

Altman J. H., 1977, in James T. H., ed., The Theory of the Photographic Process. MacMillan, New York, p. 481
Beard S. M., MacGillivray H. T., Thanisch P. F., 1990, MNRAS, 247, 311
Bland-Hawthorn J., Shopbell P. L., 1993, in IAU Commission 9: Working Group on Wide-Field Imaging, Newsletter No. 3, 52
Carter D., 1993, Gemini, No. 39, p. 14
Draper P. W., Eaton N., 1996, Starlink User Note 109: PISA: Position, Intensity and Shape Analysis
Furenlid I., Schoening W. E., Carder B. E., 1977, AAS Photo-Bulletin No. 16
Hambly N. C., Miller L., MacGillivray H. T., Herd J. T., Cormack W. A., 1998, MNRAS, in press
Hawkins M. R. S., 1991, in IAU Commission 9: Working Group on Wide-Field Imaging, Newsletter No. 1, 23
Hoaglin D. C., Mosteller F., Tukey J. W., 1983, Understanding Robust and Exploratory Data Analysis, Wiley, Chapter 11
Irwin M. J., 1996, in Espinosa J. M., ed., 7th Canary Islands Winter School, Detectors and Data Analysis Techniques for Wide Field Optical Imaging. Cambridge Univ. Press, Cambridge, p 59
Kemp S. N., Meaburn J., 1993, A&A, 274, 19
MacGillivray H. T., Thomson E. B., 1992, Digitised Optical Sky Surveys, Astrophysics and Space Science Library Proceedings, Vol. 174. Kluwer, Dordrecht
Malin D. F., 1988, in Marx S., ed., Proc. IAU Workshop on Astrophotography. Springer, Berlin, p. 125
Miller L., Cormack W. A., Paterson M., Beard S. M., Lawrence L., 1992, see MacGillivray & Thomson (1992), p. 133
Morgan D. H., Tritton S. B., Savage A., Hartley M., Cannon R. D., 1992, see MacGillivray & Thomson (1992), p. 11
Nutting P. G., 1913, Phil. Mag., 26, 423
Schwartzenberg J. M., Phillipps S., Parker Q. A., 1996, A&AS, 117, 179
Selwyn E. W. H., 1935, Photogr. J., 75, 571
Tritton S. B., 1983, UKSTU Handbook, Royal Observatory Edinburgh